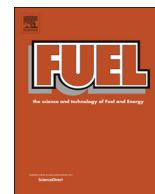




ELSEVIER

Contents lists available at ScienceDirect

Fuel

journal homepage: www.elsevier.com/locate/fuel

Full Length Article

Large eddy simulation of turbulent supersonic hydrogen flames with OpenFOAM

Huangwei Zhang*, Majie Zhao, Zhiwei Huang

Department of Mechanical Engineering, National University of Singapore, 9 Engineering Drive 1, Singapore 117576, Singapore

ARTICLE INFO

Keywords:

Shock wave
Supersonic flame
Hydrogen
Lifted flame
Supersonic combustor
OpenFOAM

ABSTRACT

A high-fidelity numerical solver, RYrhoCentralFoam, is developed based on OpenFOAM® to simulate turbulent compressible reactive flows. It is designed for accurately simulating combustion with detailed chemistry, turbulence, shock wave and their interactions. The features that we develop in this work include: (1) multi-species transport, (2) detailed fuel chemistry, and (3) turbulent combustion models in Large Eddy Simulations (LES). Two hydrogen flames with detailed measurements are studied, including turbulent auto-igniting flame in hot co-flowing jet and supersonic combustion in a supersonic burner. For the first flame, the lift-off height, overall flow and flame behaviors, as well as the statistics of the velocity and reactive scalar are computed accurately. For the second flame, the RYrhoCentralFoam is also shown to have the ability for modelling supersonic combustion in model combustors, in terms of the velocity and temperature fields as well as unsteady flame lift-off dynamics in a recirculating zone. The accuracies of LES with RYrhoCentralFOAM in both flames are comparable to those with other well-validated compressible flow solvers.

1. Introduction

In high-speed propulsion systems (e.g. scramjet), the flow physics are characterized by high Mach number and pronounced discontinuities, e.g. shock wave [1]. Meanwhile, heat release from chemical reactions may considerably modulate the localized high-speed flow fields. Furthermore, turbulence is ubiquitous in the practical combustion systems, and eddies of different scales can affect the flow and reactive fields at large- and small-scale levels. Therefore, modelling turbulent combustion under high-speed flow conditions necessitate a numerical solver which is expected to accurately handle the above interactive phenomena simultaneously.

OpenFOAM® [2] has proved to be promising for investigating various fluid mechanics problems, e.g. compressible flows and chemically reactive flows. In particular, the density-based solver, rhoCentralFoam [3], is developed for shock-laden high-speed flows, and the shocks are captured with the central-upwind Kurganov and Tadmor (KT) [4] or Kurganov, Noelle and Petrova (KNP) [5] scheme with proper slope limiters. Both schemes avoid complicated manipulations for flux calculations on polyhedral cells with arbitrary number of inter-cell faces, e.g. characteristic decomposition, Jacobian calculation and Riemann solver. Detailed validations have been made for rhoCentralFoam based on one-dimensional and two-dimensional benchmark cases [3],

including shock tube, forward-facing step, supersonic air jet, hypersonic flow over a biconic. Their results show that the KNP scheme with van Leer limiter [6] can give us accurate and non-oscillatory predictions of shock waves, through comparisons with the analytical solutions and numerical results using well-recognized schemes (e.g. Roe scheme [7]).

Large eddy simulation is a promising method for understanding the fundamentals of supersonic flows and development of practical propulsion systems [1]. It is known that, in LES with explicit filtering, capturing turbulence structures necessitates low-dissipation numerical schemes. Here explicit filtering means that the LES filter is associated with the local grid size. However, such kind of schemes with low dissipation may not perform well in capturing discontinuities embedded in the turbulent flows, such as shock waves. Therefore, how to compromise the accuracies of the selected schemes in handling both turbulence and shock wave in one flow field should be delicately evaluated. When it comes to rhoCentralFOAM, one needs to examine whether the KNP scheme can accurately predict the turbulence structures of various scales, although its ability in shock capturing have been confirmed by Greenshields et al. [3].

In recent years, various customized rhoCentralFOAM solvers have been developed for LES of turbulent combustion problems. For instance, Fan et al. simulate the supersonic flames in model scramjet combustors, and satisfactory agreements are achieved regarding the

* Corresponding author.

E-mail address: huangwei.zhang@nus.edu.sg (H. Zhang).

overall aerodynamics characteristics [8–12]. Sun et al. analyze the flame stabilization mechanisms in the supersonic combustor with rearwall-expansion cavity [13–16]. Moreover, Ye et al. and Piao et al. perform LES of a supersonic combustor and transverse hydrogen jet in a model scramjet combustor [17–19].

The foregoing studies have shown different levels of success of rhoCentralFOAM in predicting velocity, wall pressure and heat flux, etc. in supersonic flames. This is confirmed by their respective comparisons with experimental data and/or schlieren images. Nevertheless, detailed assessment of computed reactive scalars (mass fractions of major/minor species as well as temperature) are not shown in the above work. This is probably due to the unavailability of the measurements from their selected target flames. It is well acknowledged that strong flow and flame unsteadiness can be present locally or globally in supersonic combustion, for instance, reactant mixing, ignition, flame stabilization and blow-off [1]. Modelling of the above flame dynamics necessitates accurate predictions of the chemical reactions and their interactions with the local turbulence and flow features (e.g. shocks). In this sense, detailed assessments of the rhoCentralFOAM solver in predictions of reactive scalar evolutions and transient flame dynamics in turbulent supersonic flames are in high demand, if one aims to build further modules or libraries over it as an original solver.

We develop a high-fidelity and multi-physical numerical tool, grounded on rhoCentralFOAM as the framework solver, for our research interests in turbulent, compressible and reactive flows. Therefore, as a first step, we made the following implementations based on rhoCentralFoam: (1) transport of multi-component species, (2) detailed fuel chemistry, and (3) turbulent combustion models in LES (e.g. multiple mapping conditioning [20] and tabulated chemistry). For brevity, the solver is termed as RYrhoCentralFoam hereafter, in which “R” stands for “reacting” whilst “Y” means “multi-species”. It has been validated and successfully used for modelling reacting and non-reacting flows in supersonic conditions [21–24]. Recently, we use it for modelling autoignition of ethylene flames in a model scramjet configured with strut and cavity using highly-resolved LES, however, no detailed validations are made therein [25]. The objective of this work is to quantitatively assess the accuracy and applicability of RYrhoCentralFoam in modelling turbulent supersonic flames, particularly about the evolutions of the reactive scalars and the relevant flame phenomena. To this end, a sequence of benchmark cases is tested to evaluate the ability of the solver in capturing flow discontinuities (i.e. one-dimensional Sod’s shock tube, two-dimensional forward step and shock-vortex interaction), and chemical reaction (i.e. perfectly stirred reactor). The results are presented in the [Appendices A and B](#).

Besides, two turbulent supersonic flames are selected to examine the accuracies of RYrhoCentralFoam in simulating turbulent reacting flows and shock waves: (1) lifted hydrogen supersonic flame in vitiated co-flowing jet [26] and (2) strut-stabilized supersonic hydrogen flame in a model combustor [27,28]. The rationales of the foregoing selections are based on their distinct flow and combustion dynamics. Specifically, based on the experimental measurements of the first flame, the shock-train is observable and the autoigniting spots are intermittently induced by the shocks before the flame base. Turbulence also plays a significant role in initiating chemical reactions (e.g. radical build-up). From the measurements of the second flame, continuous shock reflection from the chamber walls occur. The flame is lifted and stabilized in the recirculation zone created by the strut. The shock incident, recirculating flow transport, turbulence and chemical reaction occur simultaneously behind the strut. Therefore, these two cases with various flame/flow characteristics render them ideal for evaluating RYrhoCentralFoam in modelling interactions between chemistry, turbulence and shock wave in supersonic flames.

In the rest of the manuscript, governing equations and numerical approaches in RYrhoCentralFoam solver are presented in [Section 2](#), followed by the introductions of the LES and sub-grid scale combustion models in RYrhoCentralFoam in [Section 3](#). LES of two turbulent

supersonic flames are investigated in [Section 4](#). The conclusions are summarized in [Section 5](#).

2. Governing equation and numerical method

2.1. Governing equation

The LES equations of mass, momentum, energy, and species mass fraction can be derived through low-pass filtering their respective instantaneous equations. They, together with the ideal gas equation of state, can be written as

$$\frac{\partial \bar{\rho}}{\partial t} + \nabla \cdot [\bar{\rho} \tilde{\mathbf{u}}] = 0 \quad (1)$$

$$\frac{\partial (\bar{\rho} \tilde{\mathbf{u}})}{\partial t} + \nabla \cdot [\tilde{\mathbf{u}} (\bar{\rho} \tilde{\mathbf{u}})] + \nabla \bar{p} + \nabla \cdot (\bar{\mathbf{T}} - \mathbf{T}^{sgs}) = 0 \quad (2)$$

$$\frac{\partial (\bar{\rho} \tilde{E})}{\partial t} + \nabla \cdot [\tilde{\mathbf{u}} (\bar{\rho} \tilde{E})] + \nabla \cdot [\tilde{\mathbf{u}} \bar{p}] + \nabla \cdot (\bar{\mathbf{T}} \cdot \tilde{\mathbf{u}}) + \nabla \cdot (\mathbf{j} - \mathbf{E}^{sgs}) = \bar{\omega}_T \quad (3)$$

$$\frac{\partial (\bar{\rho} \tilde{Y}_m)}{\partial t} + \nabla \cdot [\tilde{\mathbf{u}} (\bar{\rho} \tilde{Y}_m)] + \nabla \cdot (\bar{\mathbf{s}}_m - \mathbf{s}_m^{sgs}) = \bar{\omega}_m, (m = 1, \dots, M - 1) \quad (4)$$

$$\bar{p} = \bar{\rho} R \bar{T} \quad (5)$$

Here the symbol “ $\tilde{(\cdot)}$ ” denotes Favre-filtered quantities, whereas “ $\bar{(\cdot)}$ ” denotes filtered quantities. The variable t is time, and $\nabla \cdot (\cdot)$ is divergence operator. $\bar{\rho}$ is the filtered density, $\tilde{\mathbf{u}}$ is the filtered velocity vector, \bar{p} is the filtered pressure and updated from the equation of state, i.e. Eq. (5). \tilde{Y}_m is the mass fraction of m -th species, M is the total species number. Only $(M - 1)$ equations are solved in Eq. (4) and the mass fraction of the inert species (e.g. nitrogen) can be recovered from $\sum_{m=1}^M \tilde{Y}_m = 1$. The filtered total energy \tilde{E} in Eq. (3) is defined as $\tilde{E} = \tilde{e} + |\tilde{\mathbf{u}}|^2/2 + k_{sgs}$ with \tilde{e} being the filtered internal energy and k_{sgs} being the sub-grid scale kinetic energy. R in Eq. (5) is specific gas constant, calculated from $R = R_u \sum_{m=1}^M \tilde{Y}_m MW_m^{-1}$. MW_m is the molar weight of m -th species and R_u is universal gas constant. Note that the correlations between the density and temperature fluctuations are not considered in equation of state, i.e. Eq. (5).

$\bar{\mathbf{T}}$ in Eq. (2) is the filtered viscous stress tensor, modelled as

$$\bar{\mathbf{T}} = -2\mu \text{dev}(\bar{\mathbf{D}}) \quad (6)$$

μ is dynamic viscosity and is predicted with Sutherland’s law, $\mu = A_s \sqrt{T}/(1 + T_s/T)$. Here $A_s = 1.67212 \times 10^{-6} \text{kg/m}\cdot\text{s}\cdot\sqrt{\text{K}}$ is the Sutherland coefficient, while $T_s = 170.672 \text{K}$ is the Sutherland temperature. Moreover, $\bar{\mathbf{D}} \equiv [\nabla \tilde{\mathbf{u}} + (\nabla \tilde{\mathbf{u}})^T]/2$ is the deformation gradient tensor and its deviatoric component, i.e. $\text{dev}(\bar{\mathbf{D}})$, is defined as $\text{dev}(\bar{\mathbf{D}}) \equiv \bar{\mathbf{D}} - \text{tr}(\bar{\mathbf{D}})\mathbf{I}/3$ with \mathbf{I} being the unit tensor.

In addition, $\bar{\mathbf{j}}$ in Eq. (3) is the filtered diffusive heat flux and can be calculated by

$$\bar{\mathbf{j}} = -k \nabla \bar{T} \quad (7)$$

with T being the filtered temperature and k being the thermal conductivity, which is calculated using the Eucken approximation [29], $k = \mu C_v (1.32 + 1.37 \cdot R/C_v)$, where C_v is the heat capacity at constant volume and derived from $C_v = C_p - R$. Here $C_p = \sum_{m=1}^M \tilde{Y}_m C_{p,m}$ is the heat capacity at constant pressure, and $C_{p,m}$ is estimated from JANAF polynomials [30].

In Eq. (4), $\bar{\mathbf{s}}_m$ is the filtered scalar flux, which reads

$$\bar{\mathbf{s}}_m = -D \nabla (\bar{\rho} \tilde{Y}_m) \quad (8)$$

With the unity Lewis number assumption, the mass diffusivity D is calculated as $D = k/\bar{\rho} C_p$. $\bar{\omega}_m$ in Eq. (4) is the filtered net production rate of m -th species due to chemical reactions and can be calculated from the reaction rate of each elementary reaction $\bar{\omega}_{m,j}^o$, i.e.

$$\bar{\omega}_m = MW_m \sum_{j=1}^N \bar{\omega}_{m,j}^o \quad (9)$$

Here N is the number of elementary reactions, and $N > 1$ when multi-step or detailed chemical mechanism is used. The term $\bar{\omega}_T$ in Eq. (3) accounts for the heat release from chemical reactions and is estimated as $\bar{\omega}_T = -\sum_{m=1}^M \bar{\omega}_m \Delta h_{f,m}^o$. Here $\Delta h_{f,m}^o$ is the formation enthalpy of m -th species. In Eq. (4), $\mathbf{s}_m^{\text{sgs}}$ is the species transport due to the sub-grid scale velocity fluctuations, which is modelled through a gradient-type model, i.e.

$$\mathbf{s}_m^{\text{sgs}} = -\frac{\mu_{\text{sgs}}}{Sc_t} \nabla \tilde{Y}_m \quad (10)$$

where Sc_t is turbulent Schmidt number and assumed to be 1.

In Eq. (2), \mathbf{T}^{sgs} is the sub-grid scale stress tensor, and modelled as (μ_{sgs} is the sub-grid scale viscosity)

$$\mathbf{T}^{\text{sgs}} = \frac{2\bar{\rho}k_{\text{sgs}}\mathbf{I}}{3} - 2\mu_{\text{sgs}}\text{dev}(\bar{\mathbf{D}}) \quad (11)$$

Moreover, the sub-grid scale term E^{sgs} in Eq. (3) takes the following form

$$E^{\text{sgs}} = -\frac{\mu_{\text{sgs}}}{Pr_t} C_p \nabla \tilde{T} - (\mu + \mu_{\text{sgs}}) \nabla k_{\text{sgs}} + \bar{\mathbf{u}} \mathbf{T}^{\text{sgs}} \quad (12)$$

where Pr_t is the turbulent Prandtl number and assumed to be 1.

2.2. Turbulence model

In RYrhoCentralFoam, the sub-grid turbulence models include constant Smagorinsky model and one-equation model [31]. In the Smagorinsky model, the sub-grid scale stress tensor \mathbf{T}^{sgs} (see Eq. (11)) is closed with an algebraic model [31]. Specifically, the sub-grid scale viscosity μ_{sgs} is estimated from

$$\mu_{\text{sgs}} = c_k \Delta \bar{\rho} k_{\text{sgs}}^{1/2} \quad (13)$$

where the model constant c_k is 0.02, and Δ is the nominal filter size. Based on the local equilibrium assumption (i.e. production balances the dissipation), the algebraic equation can be obtained with respect to the sub-grid scale kinetic energy k_{sgs} [31]

$$\mathbf{T}^{\text{sgs}} : \bar{\mathbf{D}} + \bar{\rho} \varepsilon = 0 \quad (14)$$

where the symbol “:” denotes the double inner product of two tensors and the dissipation rate of the sub-grid scale kinetic energy, ε , is modelled as (the model constant $c_\varepsilon = 1.048$)

$$\varepsilon = c_\varepsilon \frac{k_{\text{sgs}}^{3/2}}{\Delta} \quad (15)$$

In the one-equation model, the sub-grid scale kinetic energy k_{sgs} is solved through [31]

$$\frac{\partial(\bar{\rho}k_{\text{sgs}})}{\partial t} + \nabla \cdot [\bar{\mathbf{u}}(\bar{\rho}k_{\text{sgs}})] = \nabla \cdot [(\mu + \mu_{\text{sgs}}) \nabla k_{\text{sgs}}] - \text{tr}(\mathbf{T}^{\text{sgs}}) \nabla \cdot \bar{\mathbf{u}} - \frac{C_\varepsilon \bar{\rho} k_{\text{sgs}}^{3/2}}{\Delta} \quad (16)$$

where $c_\varepsilon = 1.048$ is a model constant and $\text{tr}(\cdot)$ is the trace of a tensor.

2.3. Combustion model

In RYrhoCentralFoam, the implemented combustion models for LES include the Quasi-Laminar Chemistry (QLC), Tabulated Chemistry (TC) and Multiple Mapping Conditioning (MMC) [20] methods. For the QLC method, it neglects the effects of the reactive scalar fluctuations on the chemical reactions. Therefore, the filtered reaction rates are computed with the filtered species mass fractions and temperature [1]. The validity of this method can be justified with either of the following

possibilities. Firstly, the majority of flow kinetic energy is resolved by LES and therefore most of the fluctuations can be computed; Or secondly, the mixing timescale is much smaller than the chemical timescales. Since it does not involve any additional modelling implementations (i.e. directly solving species transport equations, i.e. Eq. (4)) and therefore rules out the uncertainties from the combustion models, this method is fairly popular in simulations of high-speed reactive flows. The QLC method will be used in this work to assess the accuracies of the solver in modelling turbulent supersonic flames.

For the TC and MMC methods, equations for mixture fraction and/or reaction progress variable need to be solved, besides Eqs. (1)–(3). Meanwhile, additional sub-models are required to estimate the unclosed terms. Therefore, in the current work aiming to validate the RYrhoCentralFoam solver itself, we will not include the discussion about them here, to avoid diluting our research objective. In fact, recently we have validated TC and MMC methods in RYrhoCentralFoam about turbulent supersonic flames [32,33], and the results are satisfactory about the predicted reactive scalars and unsteady flame dynamics. This further confirms the promising predictive abilities and compatibilities of RYrhoCentralFoam when it is interfaced with advanced combustion models.

3. Numerical method

Finite volume method is used in RYrhoCentralFoam to discretize the LES equations, i.e. Eqs. (1)–(4), over polyhedral CFD cells. Second-order backward scheme is employed for temporal discretization. The molecular and sub-grid scale diffusion fluxes are calculated with second-order central differencing scheme. The chemistry related terms in the right-hand side of Eqs. (3) and (4) are integrated with implicit Euler method. Based on our tests on hydrogen autoignition, it is shown to be computationally accurate and efficient when compared to other Ordinary Differential Equation (ODE) solvers, such as seulex [34] and L -stable embedded Rosenbrock ODE solver of third order [35]. Limited differences can be seen in the evolutions of species mass fractions and temperature predicted by implicit Euler method and the above ODE solvers. The results are presented in Appendix B.

For the convection terms, the second-order semi-discrete and non-staggered KNP [5] scheme is used. In a CFD cell FV , Gauss's divergence theorem can be written as (using the instantaneous variable notation)

$$\int_{FV} \nabla \cdot [\mathbf{u}\Psi] dV = \int_S [\mathbf{u}\Psi] dS \approx \sum_f \phi_f \Psi_f \quad (17)$$

here Ψ is a generic variable, e.g. ρ , $\rho\mathbf{u}$, ρE , and p . S denotes the surface of the CFD cell. $\phi_f = \mathbf{S}_f \mathbf{u}_f$ is the volume flux across the surface S . \sum_f in Eq. (17) means the summation over all the surfaces of the CFD cell FV .

The sum of the flux has three components [3,5]

$$\sum_f \phi_f \Psi_f = \sum_f [\alpha \phi_{f+} \Psi_{f+} + (1 - \alpha) \phi_{f-} \Psi_{f-} + \omega_f (\Psi_{f+} - \Psi_{f-})] \quad (18)$$

inward flux outward flux weighted diffusion term

where α is a weighting factor. For KNP scheme, biasness is introduced in the upwind direction, depending on one-sided local speed of sound. The first and second terms of the RHS of Eq. (18) denote the inward and outward fluxes, respectively. The third term is a diffusion term weighted by a volumetric flux ω_f , which is only required for the terms that is a part of a material derivative (e.g. $\nabla \cdot [\mathbf{u}(\bar{\rho} \tilde{\mathbf{u}})]$ in Eq. (2), $\nabla \cdot [\mathbf{u}(\bar{\rho} \tilde{E})]$ in Eq. (3), and $\nabla \cdot [\mathbf{u}(\bar{\rho} \tilde{Y}_m)]$ in Eq. (4)). It is an additional term based on the maximum propagation speed of any discontinuity (e.g. shocks and expansion waves) that may exist at a face between the interpolated values in the $f+$ and $f-$ directions [3]. To ensure the numerical stability, van Leer limiter [6] is needed for numerical flux calculations with KNP scheme.

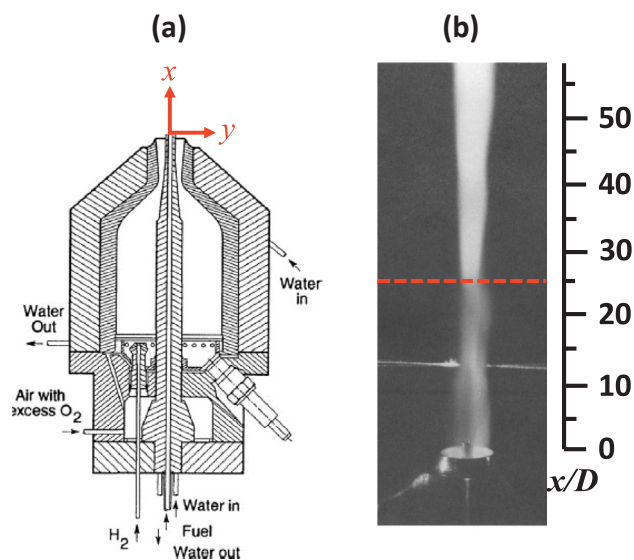


Fig. 1. (a) Schematic of the supersonic burner and (b) long exposure visual photo of the supersonic flame [26]. Dashed line denotes the measured lift-off height ($25D$, $D = 2.36$ mm is the jet diameter).

4. Results and discussion

4.1. Lifted hydrogen supersonic flames in vitiated co-flowing jet

A supersonic lifted hydrogen jet flame investigated by Cheng et al. [26] is simulated with RYrhoCentralFOAM in this Section. The burner is shown in Fig. 1. Hydrogen is sonically injected into a co-flowing supersonic vitiated air stream, and the conditions for fuel and air streams are listed in Table 1. The inner diameter of the fuel jet is $D = 2.36$ mm, whereas the inner and outer diameters of the concentric annular co-flowing jet are 3.81 and 17.78 mm, respectively. The measured flame lift-off height is $25D$, determined by the long exposure visual photograph, see Fig. 1(b) [26]. Detailed measurements include mean velocity, mean and Root-Mean-Square (RMS) values of temperature and major species concentration and also the scatters of reactive scalars at different locations [26,36]. More information about this flame can be found in Refs. [26,36]. It has also been simulated with LES using other compressible reactive solvers, including AVBP [37], SiTComb [38] and CEDRE [39], and their numerical configurations are tabulated in Table 2 for comparisons with RYrhoCentralFOAM.

A cylindrical domain of $100D \times 60D \times 2\pi$ (axial, radial and azimuthal directions, respectively) is used for LES. The coordinates origin lies at the center of the fuel jet exit with x and y for the streamwise and radial directions, respectively, as shown in Fig. 1(a). The inlet plane is at 1.18 mm upstream of the burner exit and thus a part of the fuel pipe and co-flow nozzle is included. This domain is discretized with about 26 million hexahedrons and it is refined to have a cell size of about 0.16 mm in the flame region, to ensure that the scalar mixing and unsteady auto-ignition processes in induction ($x < 20 D$) and

Table 1
Information on fuel and co-flow conditions at the burner exit.

Parameter	Unit	Fuel jet	Co-flowing jet
Pressure	Pa	112,000	107,000
Temperature	K	545	1250
Mach number	-	1.0	2.0
Velocity	m/s	1,780	1420
H ₂ mole fraction	-	1.0	0.0
O ₂ mole fraction	-	0.0	0.201
N ₂ mole fraction	-	-	0.544
H ₂ O mole fraction	-	-	0.255

Table 2
LES of supersonic lifted hydrogen jet flame.[†]

Numerical Solver	Combustion model and chemistry	Spatial scheme	Temporal scheme	Mesh resolution	Computational domain	Reference
AVBP [37]	Quasi-laminar chemistry 5 species, 3 reactions	3rd order Taylor Galerkin	3rd order Runge-Kutta	6.6 million cells, minimum size 0.1 ~ 0.4 mm	Hemisphere domain with 0.85D off burner exit and radius 10,000D	[41]
SiTComb [38]	Quasi-laminar chemistry 5 species, 3 reactions	Blended 2nd and 4th artificial dissipation terms	4th order Runge-Kutta	Three meshes: 4, 32 and 268 million cells, with minimal cells 0.24-0.86 mm, 0.12-0.43 mm and 0.06-0.215 mm	Cylindrical domain (70D × 30D × 30D) starting in the fuel injection plane	[42]
CEDRE [39]	U-PaSR 9 species, 19 reactions	2nd order HLLC/MUSCL	2nd order Runge-Kutta	31 million cells with minimal cell 0.2 mm	Cylindrical domain, detailed nozzle configuration included	[40]
CompReal	Eulerian LES-PDF 9 species, 19 reactions	Hybrid 11-2 DRP scheme and HLLC, 2nd order central differencing	1st or 3rd order Euler-Mariyama scheme	0.2 and 2 million cells	Cylindrical domain (70D × 60D × 60D)	[43]
RYrhoCentralFOAM [3]	Quasi-laminar chemistry 9 species, 1 reactions	KNP scheme with van Leer limiter	2nd order backward scheme	26 million with minimal cell size 0.16 mm	Cylindrical domain (70D × 60D × 60D)	-

[†] Smagorinsky model is used in the all the LES [40-43].

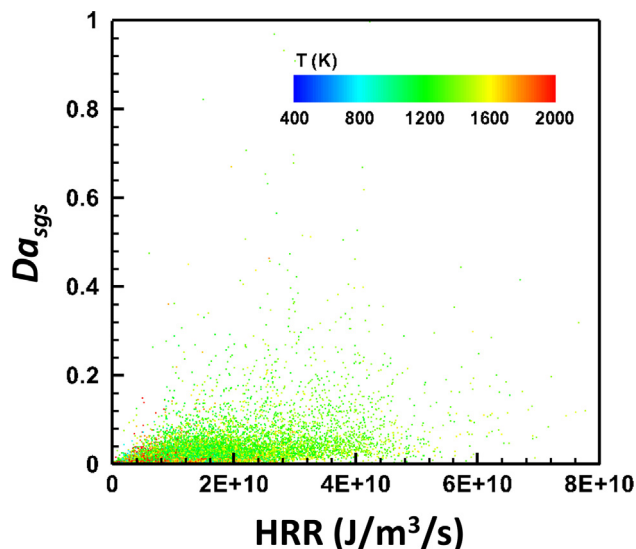


Fig. 2. Scatter plot of sub-grid Damkohler number versus heat release rate colored by temperature in the central region of $44D \times 5D \times 2\pi$.

stabilization ($20D < x < 40D$) zones can be accurately predicted [40]. This cell size is around 8–16 Kolmogorov scale (0.01–0.02 mm [26]) and is comparable to those used by Boivin et al. with 0.1–0.4 mm [41], Bouheraoua et al. [42] with 0.06–0.24 mm and Moule et al. [40] with 0.2 mm, as tabulated in Table 2. A *posteriori* analysis of the present LES results shows that the ratio of the sub-grid scale to molecular viscosities, μ_{sgs}/μ , is generally below 2 in both induction and stabilization regions, indicating that the flow kinetic energy is well resolved in our simulation.

The constant Smagorinsky model [31] detailed in Section 2.2 is used to close the sub-grid scale stress, consistent with those in Refs. [40–43]. Moreover, same as in Refs. [40–42] for modelling the same flame, the QLC method is used here to calculate the filtered chemical reactions. Its validity can be confirmed by the low sub-grid scale Damköhler numbers $Da_{sgs} = \tau_{sgs}/\tau_c$ [42] based on our LES results. Here we estimate the characteristic time of the smallest resolved structure (τ_{sgs}) and characteristic chemical time scale τ_c following Bouheraoua et al. [42]. Fig. 2

shows the scatter plot of the SGS Damköhler number Da_{sgs} versus heat release rate colored by temperature in the central region of $44D \times 5D \times 2\pi$. It is found that SGS Damköhler number is much less than unity, which suggests that the characteristic scales of chemistry are sufficiently resolved. The time step, 10^{-9} s, is used to ensure that the Courant number is less than 0.1 in the entire domain. Detailed mechanism (including 19 elementary reactions and 9 species, i.e. H_2 , O_2 , N_2 , OH , H , HO_2 , H_2O , O , H_2O_2) [44] is used here for hydrogen combustion.

The boundary conditions of fuel and co-flowing jet streams are specified following the conditions in Table 1. Top hat profiles are specified for the mean inlet velocities and the turbulence is specified using white noise with 5% intensity. Due to the lack of the measured turbulence at the inlet [26,36], attempt to specify turbulence for both inlets would induce difficultly quantified uncertainties and therefore is not made in this work. Adiabatic non-slip wall condition is used for the fuel pipe and co-flow nozzle walls. Non-reflective boundary condition is used for lateral and outlet boundaries of the cylindrical domain. A quiescent flow at 1 atm and 298 K is set as the initial field. A fully developed non-reacting flow field is first simulated with chemistry related terms deactivated, and then combustion modelling proceeds after the chemistry related terms are on.

The statistics presented in this Section below, including velocity, temperature and species mole fractions, are compiled over 0.3 milliseconds (over 3 flow-through times) after the initial field effects are purged (after 0.6 milliseconds, about 5 flow-through times). Here the flow-through time is estimated based on domain length (100D) and co-flow bulk velocity (1420 m/s). A simulation for physical time of 0.03 milliseconds takes about 24 h using 192 processors.

The contours of resolved temperature, OH and H_2O mass fractions are shown in Fig. 3(a)–(c). It is seen from Fig. 3(a) that the temperature starts to increase beyond 1600 K at around $x/D = 20$, which approximately corresponds to the instantaneous flame base location. This can also be confirmed by the considerable OH mass fraction at the similar location in Fig. 3(b). The flame base is observed to fluctuate between $10D$ and $25D$ due to the unsteady jet flow behaviors, which can be confirmed by the distributions of the mass fraction of the H_2 auto-ignition precursor radical resolved HO_2 . Similar unsteady behaviors are also reported in Refs. [42] and [40]. The predicted mean lift-off height is around $24.4D$, determined by the axial distance at which the mean

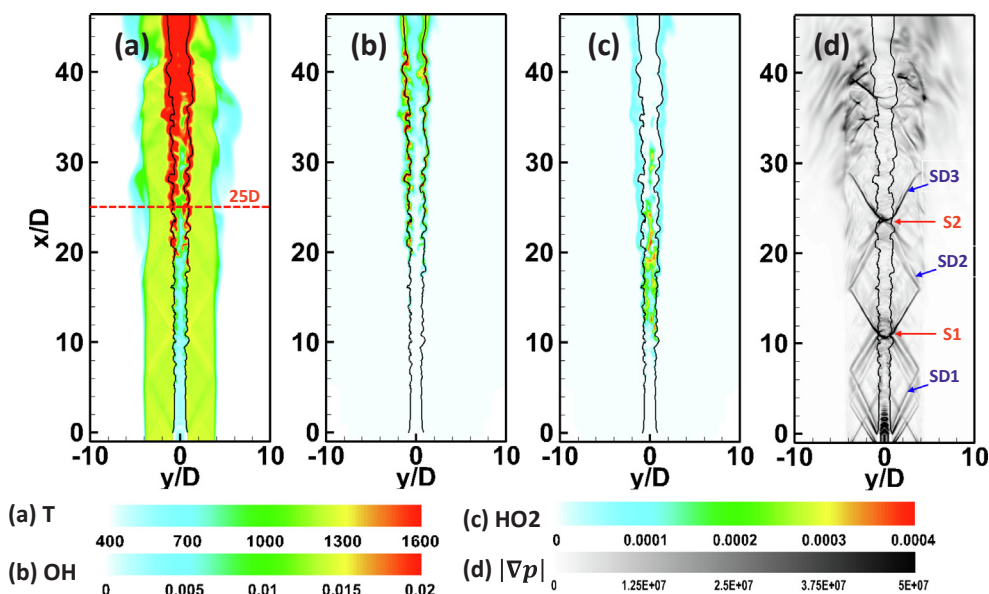


Fig. 3. Distributions of resolved (a) temperature (in K), (b) OH mass fraction, (c) HO_2 mass fraction, and (d) magnitude of pressure gradient $|\nabla p|$ (in Pa/m). Black iso-lines: stoichiometry. “SD” represents the shock diamond and “S” denotes the V-shaped shocks. The dashed line in (a) indicates the lift-off height ($25D$) from the experiments [26].

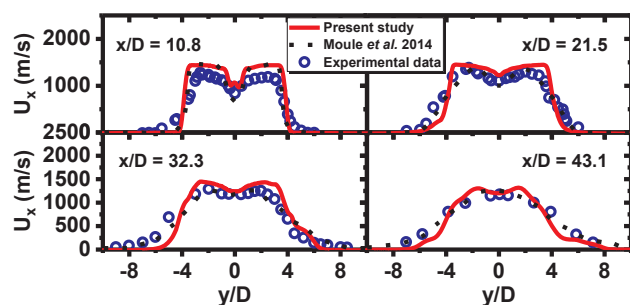


Fig. 4. Radial profiles of mean axial velocity. Experimental data from Ref. [26], and LES data from Ref. [40].

temperature exceeds 1600 K, closer to the measured $25D$ compared to those ($15D$ – $35D$) from other LES in Table 2 [40–43].

Fig. 3(d) shows the distribution of the flow structure quantified by the norm of the instantaneous pressure gradient, $|\nabla p|$. The diamond shocks in the co-flowing stream are clearly visible, consistent with the observations in Refs. [40,42]. The two connected and equal-sized diamonds, i.e. $SD1$ and $SD2$ in Fig. 3(d), start from the jet exit and end at around $22D$. Two strong V-shaped shocks $S1$ and $S2$ are formed in the jet flows (see Fig. 3d) at around $11D$ and $22D$. Downstream of $S1$, the elevated pressure and temperature lead to pronounced chemical reactions, indicated by the considerably increased HO_2 . Beyond the induction zone ($x/D = 20$), the flame has appeared, featured by higher temperature and OH (see Fig. 3a and b). $S2$ is close to the averaged flame stabilization point, indicating that $S2$ may play significant role in stabilizing supersonic H_2 flame. Further downstream, the diamond shock $SD3$ becomes blurred and only the half is observable, probably due to its interactions with local turbulence and/or co-flowing stream instabilities.

Fig. 4 shows the radial profiles of mean axial velocity at $x/D = 10.8, 21.5, 32.3$ and 43.1 . Excellent agreement with the experimental data [26] is observed regarding the magnitudes and shapes of the profiles. However, the velocity in the co-flow at $x/D = 10.8$ is slightly over-predicted (by about 10%). This discrepancy is also seen from the LES results by Moule et al. [40], where the detailed nozzle configuration is included. It may be caused by the fact that the velocity profile and turbulence at the burner exit do not exactly mimic the conditions in the experiment. In general, our LES accurately reproduces the flow field in both induction ($x < 20D$) and stabilization ($20D < x < 40D$) zones of this flame.

The radial profiles of mean temperature and the RMS are presented for $x/D = 10.8, 21.5, 32.3$ and 43.1 in Fig. 5. For comparisons, the LES data predicted by SiTComb [38] and CEDRE [39] are also included with their numerical details listed in Table 2. It should be noted that the measured temperatures at the foregoing locations are asymmetric due to a small tilt in the burner arrangement [26]. Understanding this experimental uncertainty, we can see that the present LES results predict the temperature distributions reasonably well, particularly for the locations of $y < 0$. At $x/D = 10.8, 21.5$ and 32.3 , the difference between different LES is very small. At $x/D = 43.1$, the mean temperature is underestimated in our LES, which is also observed in the results of Refs. [40,42].

The temperature RMS in the central flame region and the interface between the co-flowing jet and the surrounding gas are predicted generally satisfactorily, as demonstrated in Fig. 5. Nevertheless, the fluctuations in the co-flowing jet is under-predicted, particularly for the upstream locations (i.e. $x/D = 10.8$ and 21.5). This may be caused by the specifications of the turbulent inlet conditions, or not sufficiently fine meshes to capture the temperature fluctuations. Note that Bouheraoua et al. [42] used fairly fine mesh (see Table 2) and the RMS is considerably overshoot, while for the upstream locations (e.g. $x/D = 10.8$) improved prediction can be found. The RMS differences are

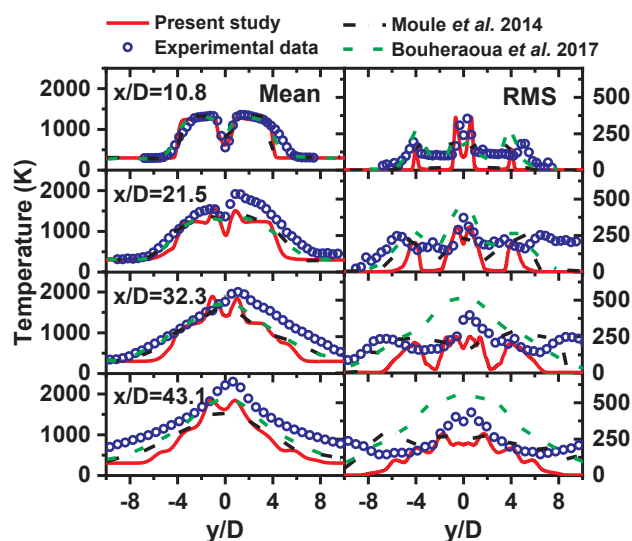


Fig. 5. Radial profiles of mean temperatures and the RMS. Experimental data from Ref. [26], and LES data from Refs. [40,42].

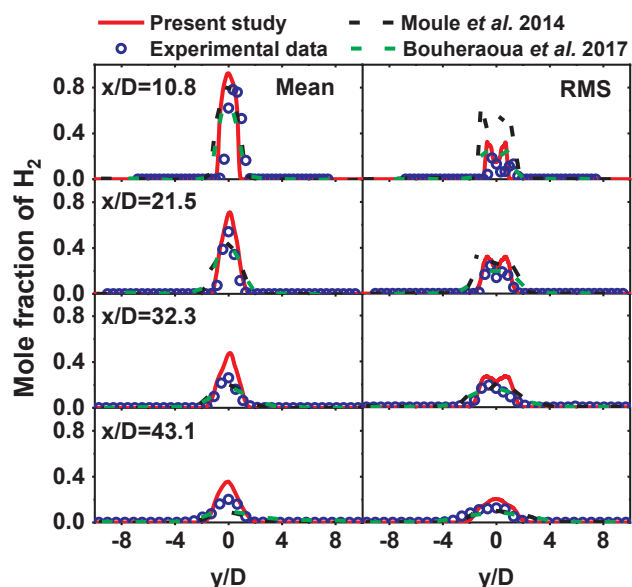


Fig. 6. Radial profiles of mean H_2 mole fraction and the RMS. Experimental data from Ref. [26].

also seen from the LES of Moule et al. [40], indicating their strong sensitivity to the LES numerics.

The radial profiles of H_2 and H_2O mole fractions are shown in Figs. 5 and 6 for the same four axial locations. Moreover, the LES data from Refs. [40,42] has been added for comparison in Figs. 6 and 7. Although slightly differences are observed with different solvers, mean mole fractions of H_2 and H_2O species show excellent agreement with the experimental data [26]. The differences from different LES may be due to the different inlet turbulent boundary conditions and mesh resolutions. The results shown in Figs. 6 and 7 suggest that the quasi-laminar chemistry method can predict the temperature and major species mole fractions reasonably well in the current LES studies.

Scatter plots of temperature and mole fractions of H_2 , H_2O and OH against mixture fraction are presented in Figs. 8 and 9 for two locations, $(x/D, y/D) = (10.8, 0.65)$ and $(32.3, 1.1)$, respectively. The first location lies in the induction zone and thus the computed H_2 and H_2O mole fractions roughly follow the mixing line. The flow in this region is dominated by the large scale mixing. There is no salient OH at this

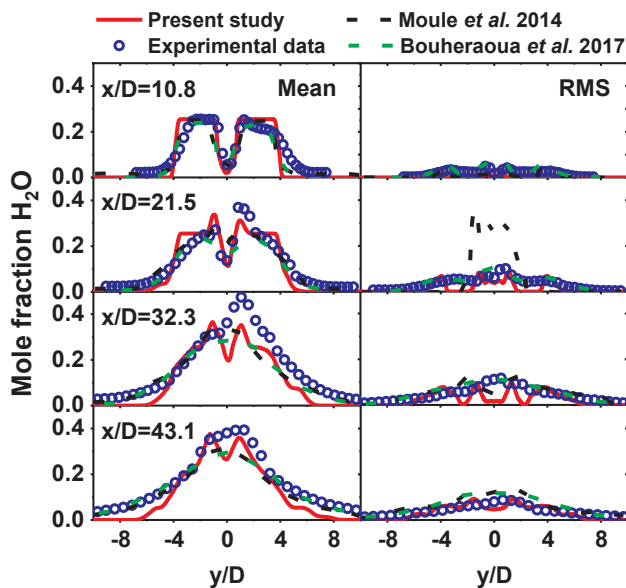


Fig. 7. Radial profiles of mean H₂O mole fraction and the RMS. Experimental data from Ref. [26].

location from the LES, in line with the experimental results. However, low OH mole fraction (< 0.005) for very low mixture fractions (< 0.04) are observed in the experiments, which may be due to the fuel-lean pre-combustion products of hot co-flow jets [26]. Therefore, the chemical reaction is slightly under-predicted at this location (see the slightly lower temperature in Fig. 3a). Moule et al. [40] observed finite OH for this location in their simulation, but for a shifted (0.01–0.06) mixture fraction range. This may be due to the reason that the detailed nozzle configuration was included in Ref. [40], suggesting that the variations of OH concentration and temperature in the induction zone are sensitive to the flow conditions at the burner exit. This may be affected by near-field scalar mixing, further subject to the inlet boundary condition. A complete assessment of this uncertainty requires experimental characterization of the inflow turbulence condition,

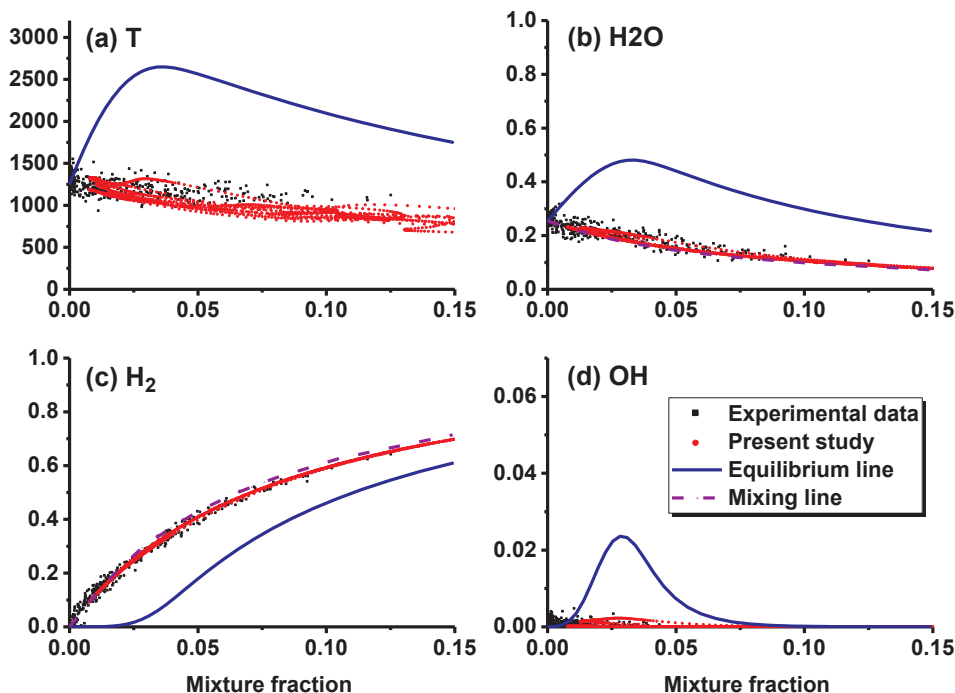


Fig. 8. Scatter plots of temperature and species mole fractions at one probed location, i.e. $x/D = 10.8$ and $y/D = 0.65$. Solid line: equilibrium flame solutions [26]; dashed line: mixing solutions [26]; black dots: experimental data [26]; red dots: LES. (For interpretation of the references to colour in this figure legend, the reader is referred to the web version of this article.)

which was not measured by Cheng et al. [26] in the experiments.

Fig. 9 shows the scatter plot for $(x/D, y/D) = (32.3, 1.1)$, which is beyond the measured lift-off height, i.e. about $25D$ [26]. Overall, the simulation results agree well with the measured ones. Compared to the results in Fig. 8, the species mole fractions are closer to, or scatter around, the equilibrium solutions, indicating the pronounced chemical reactions proceeding at this location. Two features are worth noting. Firstly, the computed mixture fraction varies approximately from 0 to 0.1, slightly larger than the measured range 0–0.08, but it is still consistent with the results in Refs. [40]. Secondly, the fluctuations in temperature and three species mole fractions are under-predicted. These under-predictions are also observed in Refs. [40,42]. In general, Figs. 8 and 9 show that the reactive scalars in mixture fraction space at both induction and stabilization zones are well captured.

Through the above LES of autoigniting supersonic hydrogen flames with RYrhoCentralFOAM, one can conclude that: (1) the shock wave structure and flame lift-off height can be predicted accurately; (2) the statistics of velocity, temperature, major species concentration are correctly captured; (3) the thermochemical structures in both induction and stabilization zones are simulated reasonably well. It is also seen that the accuracies of LES with RYrhoCentralFOAM in this flame are comparable to other well-known compressible solvers listed in Table 2. Note that the vitiated air stream with stagnation conditions of 778,000 Pa and 1750 K is accelerated through a convergent-divergent nozzle from a combustion chamber, and may have some turbulent fluctuations which are not measured in the experiments [26]. Therefore, the uncertainties from the turbulence in the supersonic co-flows may be one of the major reasons for the underestimating the reactive scalar fluctuations. The effects of turbulence inlet conditions on supersonic flame autoignition and stabilization should be further assessed through future LES and experimental studies.

4.2. Supersonic hydrogen flames in a model combustor

A hydrogen-fueled strut model supersonic combustor, experimentally studied in DLR [27,28], will be investigated in this Section. Its main flame/aerodynamic features and its difference from the preceding flame has been described in Section 1. The two-dimensional configuration is schematically shown in Fig. 10. The combustor consists of a

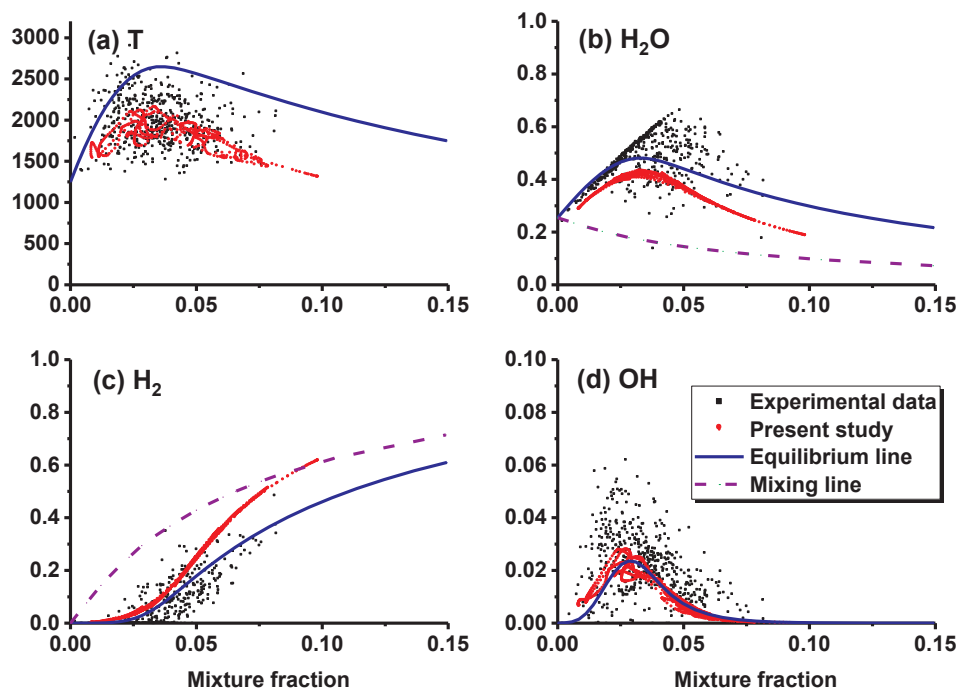


Fig. 9. Scatter plots of temperature and species mole fractions at one probed location, i.e. $x/D = 32.3$ and $y/D = 1.1$. Legend for lines and symbols is same as that for Fig. 8.

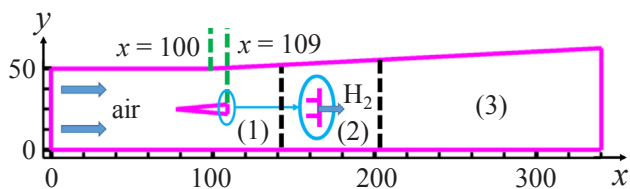


Fig. 10. Two-dimensional schematic of the DLR combustor [2728]. Dimension in mm. Zone (1): induction zone; (2): transitional zone; (3): turbulent combustion zone.

one-sided divergent channel and a wedge-like flame stabilizer (or strut interchangeably hereafter). The combustor is 50 mm in height (i.e. y -direction) at the entrance, 340 mm in length (i.e. x -direction), and 45 mm in width (i.e. z -direction, not shown in Fig. 10). The strut is 32 mm in length and 6 mm in height, with the same width as that of the combustor. It is placed at the centerline of the combustor at 77 mm downstream to the entrance [27,28], and its rear lies at $x = 109$ mm. Moreover, the 15 circular fuel injectors (each 1 mm in diameter) lie at the rear of the strut. The upper wall has a divergence angle of 3° since $x = 100$ mm to compensate for the boundary layer expansion. The flow field of this combustor is characterized by a subsonic triangular recirculation zone (longitudinal length 40 mm or so) behind the strut, embedded in a supersonic free stream [27,28]. Three salient zones are present, depending on the degree of local chemical reactions and flow/mixing fields, which include (1) induction zone, (2) transitional zone (i.e. $142 \text{ mm} < x < 203 \text{ mm}$) and (3) turbulent combustion zone [27,28], as shown in Fig. 10. The measurements include PIV and LDV measurements of velocity and CARS measurements of temperature [27,28], which are conducive for CFD validations.

In the experiments [27,28], the air, from a preceding Laval nozzle section, enters the combustor at a supersonic speed ($Ma = 2.0$) with total temperature (T^*) of 600 K and static pressure (p) of 0.1 MPa, respectively. Note that the hot air is vitiated with H_2O addition (3.2% w.t.). The pure hydrogen is injected sonically with total temperature of 300 K and static pressure of 0.1 MPa. The global equivalence ratio (ϕ) is

Table 3

Conditions of air and hydrogen streams.

Inlet	u_x [m/s]	T^* [K]	p [MPa]	Ma	Y_{O_2}	Y_{N_2}	Y_{H_2O}	Y_{H_2}	ϕ
air	730	600	0.1	2.0	23.2%	73.6%	3.2%	0.0	0.034
H_2	1,200	300		1.0	0.0	0.0	0.0	100%	

0.034. The information of the operating conditions at both streams is summarized in Table 3.

It has been found from the previous work [33,45] that the spanwise interactions between the aerodynamic phenomena (e.g. shocks, expansion fans and shear layers) behind the originally 15 circular fuel injectors are small. This can be further confirmed by our recent studies on the same combustor based on two-dimensional domain with RYrhoCentralFOAM [23,46]. Therefore, in this LES, to reduce the computational cost, only one fuel injector is considered and the spanwise dimension (as mentioned at the beginning of this Section) is also proportionally reduced. The validity of this treatment has been confirmed in our recent LES work [33] and by others [45] on this combustor, where the main flow and flame dynamics in this combustor show good agreement with the experimental measurements.

The domain in Fig. 10 is discretized with static 4,866,900 hexahedrons. Local refinement is made near the fuel inlets and in the recirculation zone behind the strut, and the minimum cell is about 0.07 mm. No refinement is made near the combustor walls to resolve the near-wall turbulence, since it is assumed that this turbulence has negligible influences on the main combustion zone behind the strut [33,45]. The grid resolution effects on the velocity and temperature statistics with the same domain has been performed in our recent work [33] and, besides the existing mesh, additional two meshes with finer and coarser resolutions are tested. The results show that the current mesh can accurately reproduce the experimental measurements of velocity statistics. Details about the mesh sensitivity analysis are provided in Appendix C. Furthermore, this resolution is comparable with other LES of the same combustor [45,47], and therefore is expected to be sufficient for our current analysis.

In this LES, the sub-grid scale kinetic energy k_{sgs} is solved with the

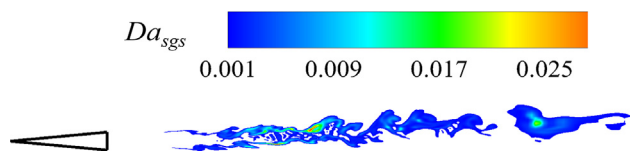


Fig. 11. Contour of sub-grid scale Damköhler number in the combustion zone.

transport equation, i.e. Eq. (19) [31], which further closes the sub-grid scale stress. Similar to Section 4.2, QLC method is used for calculating the filtered chemical reactions. The contour of the sub-grid scale Damköhler number Da_{sgs} [42] based on our LES results is shown in Fig. 11. Apparently, $Da_{sgs} \ll 1$ is valid for most of the combustion area behind the strut, which suggests that the chemical time scales are well resolved and the suitability of the QLC method in our LES.

The boundary conditions for both fuel and air inlets follow the experimental conditions tabulated in Table 3. At the outlet, the relevant variables are extrapolated from the interior cells, and non-slip wall is specified for the strut wall while slip wall is used for the combustor wall. The shock-boundary-layer interactions on the combustor walls are not resolved, because they are expected to have little effects on the central combustion regions, based on the previous studies [23,33,45,46]. The time step is 10^{-9} s, such that the Courant number is < 0.1 . Detailed mechanism (including 27 elementary reactions and 9 species, i.e. $H_2, O_2, N_2, OH, H, HO_2, H_2O, O, H_2O_2$) [48] is used. The statistics are compiled over 3.0 milli-seconds, over six flow-through time (estimated based on the combustor length and air inlet velocity), after the initial field effects diminish (after 0.6 milli-seconds). A simulation for physical time of 0.1 milli-seconds using 96 cores takes about 24 h. Also, LES of the same combustor with other solvers by Fureby and Menon and their co-workers [49–51] will be incorporated, wherever necessary, for accuracy comparisons, and their numerical information is listed in Table 4.

Fig. 12 shows the contours of instantaneous temperature and time-averaged magnitude of density gradient from LES, as well as the experimental schlieren image [27]. Flame lift-off with a mean lift-off distance (defined as the streamwise distance between the flame base location and the strut base) of 30 mm is well captured, as shown from Fig. 12(a), in line with the results, 31 mm, predicted by others (e.g. Refs. [52]). Flow structures including shocks, expansion fans, and shear layers between the central recirculation zone and the incoming supersonic air stream in Fig. 12(b), are evident and bear close resemblance to the experimental schlieren image [27] in Fig. 12(c).

Fig. 13 shows the comparisons of the time-averaged temperature with the experimental data at three streamwise locations behind the strut. Good agreements can be observed about the temperature spatial profiles for all the shown locations. Nevertheless, the peak values at $x = 167$ mm and 275 mm are under-predicted with the relative errors 12.3% and 25.8%, respectively. This may be caused by the detailed mechanism with 27 reaction steps we use here, which involves more endothermic reactions compared with the works using 5 s/2r global [49] or 7 s/7r reduced mechanisms [50,51]. Considering the possible experimental uncertainties, if a global or reduced mechanism gives good predictions in the peak temperature, then the under-predictions with a detailed mechanism can be expected. Also, the combustion model used could affect the prediction of temperature, which does not consider the sub-grid scale contributions in our simulations. Moreover, compared with the LES results by Fureby et al. [49] and Menon et al. [50] (refer to Table 4 for their LES details), at $x = 120$ mm, our results are close to those by Menon et al. [50], in which two fuel injectors are considered. Further downstream, the three LES show various levels of accuracies in temperature prediction, which may be related to the different sub-grid scale combustion models used.

Plotted in Figs. 14 and 15 are comparisons of the statistics of the axial velocity against the experimental data. The mean axial velocities and their RMS values in the recirculation zone are well predicted at

Table 4
LES of DLR strut-stabilized supersonic hydrogen flame.

Numerical Solver	Combustion model and chemistry	Turbulence model	Spatial scheme	Temporal scheme	Mesh resolution	Computational domain	Reference
Customized OpenFOAM solver	PaSR model 7 species, 7 reactions	Mixed model (scale similarity model and diffusive sub-grid viscosity model)	High-order reconstruction for convection flux, central differencing for diffusion flux	2nd order Runge-Kutta scheme	6.3 million (3 injectors) and 22.5 million (15 injectors) cells 3.2 and 6.4 million cells,	Full (15 injectors) and (3 injectors) partial width of the combustor 3 fuel injectors	[51] [49]
In-house LES solver	Flamelet model (mixture fraction/reaction progress variable) 5 species, 2 reactions Eddy dissipation concept 7 species, 7 reactions	Transport equation for sub-grid kinetic energy, localized dynamic closure	HLLC for flux reconstruction, 4th order central differencing for diffusion flux	2nd predictor/corrector time integration	2.5 million cells	2 fuel injectors	[50]
RYrhoCentralFOAM	Quasi-laminar chemistry 9 species, 27 reactions	Transport equation for sub-grid kinetic energy	KNP scheme with van Leer limiter	2nd order backward scheme	4.87 million cells	1 fuel injector	-

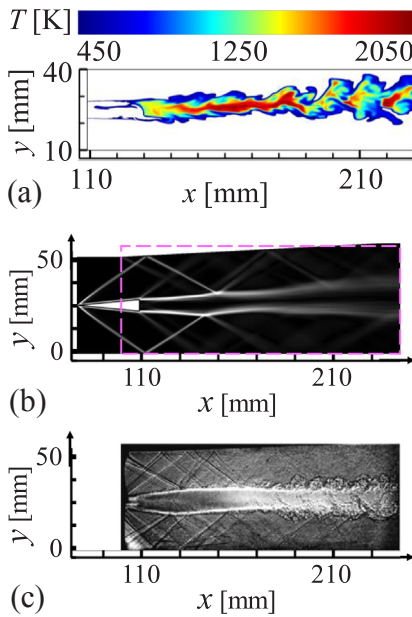


Fig. 12. Contours of (a) temperature, (b) magnitude of density gradient and (c) experimental schlieren image [27].

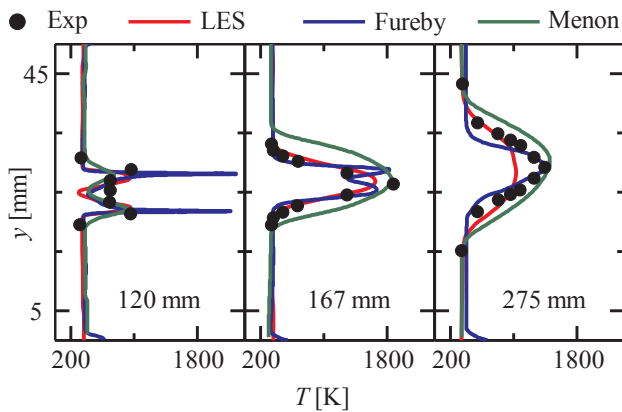


Fig. 13. Comparisons of time-averaged temperature with the experimental data [27]. LES data are from Fureby et al. [49] and Menon et al. [50].

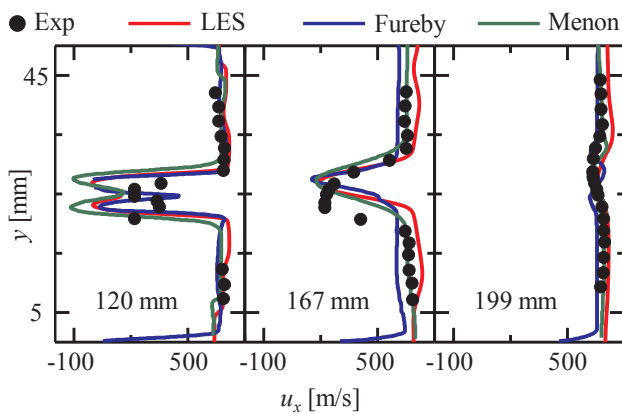


Fig. 14. Comparisons of time-averaged axial velocity with the experimental data [28]. LES data are from Fureby et al. [49] and Menon et al. [50].

= 120 mm. Meanwhile, the differences from the different LES results are not pronounced, in which the mesh resolutions are close and the transport equation for sub-grid scale kinetic energy is solved.

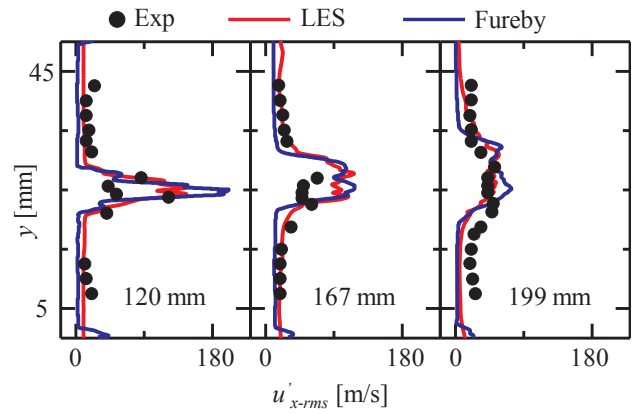


Fig. 15. Comparisons of axial velocity RMS with the experimental data [28]. The other LES data are from Fureby et al. [49].

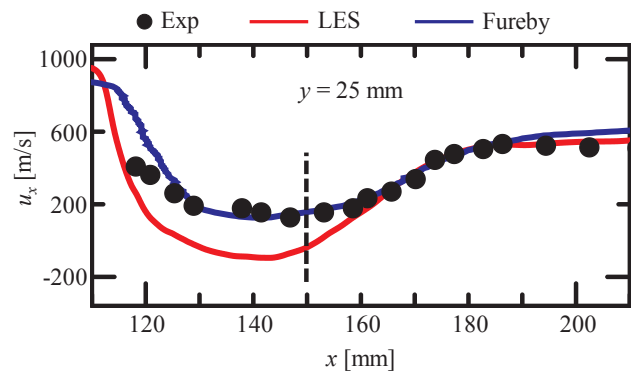


Fig. 16. Centerline profiles ($y = 25$ mm) of time-averaged axial velocity. Experimental data from Ref. [27]. LES data are from Fureby et al. [51]. The dashed line indicates the end ($x = 149$ mm) of the recirculation zone.

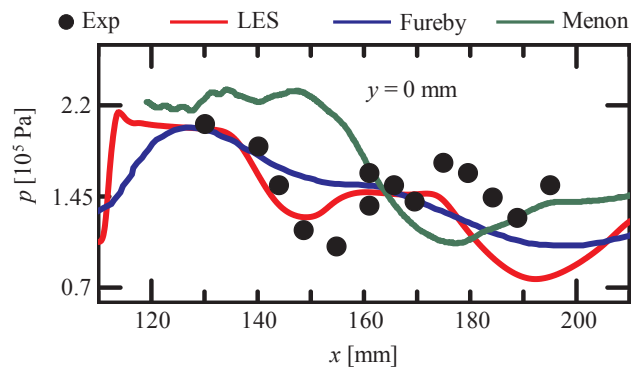


Fig. 17. Profiles of time-averaged pressure at the bottom wall of the combustor ($y = 0$ mm). Experimental data from Ref. [27]. LES data are from Fureby et al. [51] and Menon et al. [50].

Figs. 16 and 17 show the profiles of time-averaged axial velocity on the centreline and bottom wall pressure along the streamwise direction of the combustor. It can be seen from Fig. 16 that the time-averaged axial velocity predicted by our LES is lower than the experimental data when $x < 160$ mm. Beyond this range, excellent agreement is achieved. In the LES results by Fureby and his co-workers [51], they agree well with measured data for a wider range (since $x > 130$ mm). In spite of this, slight over-prediction of the time-averaged axial velocity still occurs when $x < 130$ mm in their results.

For the time-averaged pressure on the bottom wall, the discrepancies between our LES and the experimental data are more pronounced, although the pressure magnitudes are still close to each other.

These differences may result from the following reasons. Firstly, the preceding Laval nozzle section is not included in the LES, which is experimentally used to achieve a uniform supersonic air inflow. This is also the case for the work of Menon et al. [50] and Fureby et al. [51]. Hence, the wall boundary layer transition point from laminar to turbulent flows cannot be well captured in these numerical studies. It is found in Fig. 17 that pressure fluctuations generally occur earlier in the experiment than in any shown numerical work, which indicates an earlier laminar-to-turbulent transition in the experiment. Secondly, the shock-boundary-layer interactions on the combustor walls are not resolved in our LES as well as in the work of Menon et al. [50], which requires probabilistically high resolutions near the wall. However, in the work by Fureby et al. [51], the grid is clustered toward the combustor wall and a wall model [53] is applied. Nevertheless, their mesh resolution is still not small enough to accurately resolve the boundary layer. In this sense, no superiority of the LES results in Fig. 17 can be claimed. Similar difficulties in properly capturing the shock-boundary-layer interactions are also noticeable in other LES investigations [12,33]. These observations, to some degree, indicates that common difficulties exist in LES to predict the pressures on the combustor surfaces, on which different aerodynamic characteristics (e.g. shock wave, expansion wave and boundary layer) interact. However, generally, RYrhoCentralFOAM is accurate for modelling supersonic flames in model supersonic combustors.

The following observations can be made for RYrhoCentralFOAM based on the simulations in this Section: (1) the recirculating flows, shock waves, expansive waves and their interactions are well captured; (2) the flame lift-off and stabilization in the recirculation zone are correctly reproduced; (3) the velocity and temperature statistics of this flame are predicted accurately. However, predictions of the shock-boundary-layer interactions and wall pressure are largely affected by the resolution of the boundary layer in supersonic flows. This needs our further studies using a wall-resolved LES with RYrhoCentralFOAM, when the near-wall features (for instance, pressure or heat flux) are concerned in supersonic flames in a chamber.

5. Conclusions

A high-fidelity numerical solver, RYrhoCentralFoam, is developed based on OpenFOAM® to simulate turbulent compressible reactive flows. It is based on finite volume discretization on polyhedral cells and has overall second-order temporal and spatial accuracies. The newly introduced features include: (1) multi-species transport, (2) detailed fuel chemistry, and (3) turbulent combustion models in LES. To examine the prediction accuracy of RYrhoCentralFoam, one- or two-dimensional benchmark tests are performed, and two turbulent

Appendix A. Comparison of the shock capturing schemes

A.1. Sod's shock tube problem

The Sod's shock tube problem [54] is used for comparing the dissipation of KNP [5] and Roe [7] schemes. The one-dimensional Euler equations for a compressible fluid (with specific heat ratio $\gamma = 1.4$). The length of the computational domain is $L_x = 1$ m, and it is discretized with 1,000 uniform cells. The CFL number is 0.02, corresponding to a physical time step of about 10^{-8} s. The initial conditions are

$$(\rho, u, p) = \begin{cases} (1, 0, 1), & x \leq 0.5m \\ (0.125, 0, 0.1), & x > 0.5m \end{cases} \quad (\text{A1})$$

Fig. A1 shows the comparison of the results with KNP scheme and analytical solutions for density, pressure, velocity and Mach number at $t = 0.007$ s. The results obtained from the Roe scheme [7] are also shown. Our results with KNP scheme are very close to the analytical solutions and those with Roe scheme. Hence, the KNP scheme shows good accuracy in capturing the flow discontinuities.

A.2. A Mach 3 wind tunnel with a forward step

A Mach 3 wind tunnel with a forward step is used to examine the KNP scheme [5]. The wind tunnel is 1 m in height (y -direction) and 3 m in length (x -direction), whereas the step is 0.2 m in height locating at 0.6 m downstream of the entrance. A right-moving flow of Mach 3.0 enters the

supersonic hydrogen flames are simulated, i.e. turbulent auto-igniting flame in hot co-flowing jet and supersonic flame in supersonic burner.

For turbulent auto-igniting flame in hot co-flowing jet, the lift-off height, general flow and flame behaviors, as well as the mean velocity and reactive scalars are computed accurately, although some discrepancies are seen about the RMS values. Moreover, the thermochemical structures in both induction and stabilization zones are simulated reasonably well. In addition, RYrhoCentralFoam is also used for LES of recirculating supersonic flame in a model combustor. It is shown that the recirculating flow field and its interaction with the incident shock waves can be captured well. Also, the velocity and temperature statistics of this flame are predicted accurately through comparisons with the experimental data. It is also seen that the accuracies of LES with RYrhoCentralFOAM in both flames are comparable to those with other well-validated and widely used compressible solvers from other research teams, and therefore RYrhoCentralFOAM is promising for studying more problems related to turbulent supersonic combustion.

Nevertheless, based on the results of the two target flames, the effects of the turbulence in supersonic inlet flows on the flame auto-ignition and stabilization, as well as shock-boundary-layer interactions in model combustor should be further evaluated in the LES with RYrhoCentralFOAM as our future work.

CRedit authorship contribution statement

Huangwei Zhang: Writing - review & editing, Supervision, Project administration, Funding acquisition. **Majie Zhao:** Conceptualization, Methodology, Writing - original draft, Visualization, Investigation. **Zhiwei Huang:** Conceptualization, Methodology, Writing - original draft, Visualization, Investigation.

Declaration of Competing Interest

The authors declare that they have no known competing financial interests or personal relationships that could have appeared to influence the work reported in this paper.

Acknowledgements

The computational work for this article was fully performed on resources of the National Supercomputing Centre, Singapore (<https://www.nsc.sg>). The authors thank Professor R.W. Pitz from Vanderbilt University and Professor T.S. Cheng for from Chung Hua University for sharing the experimental data of the hydrogen jet flame.

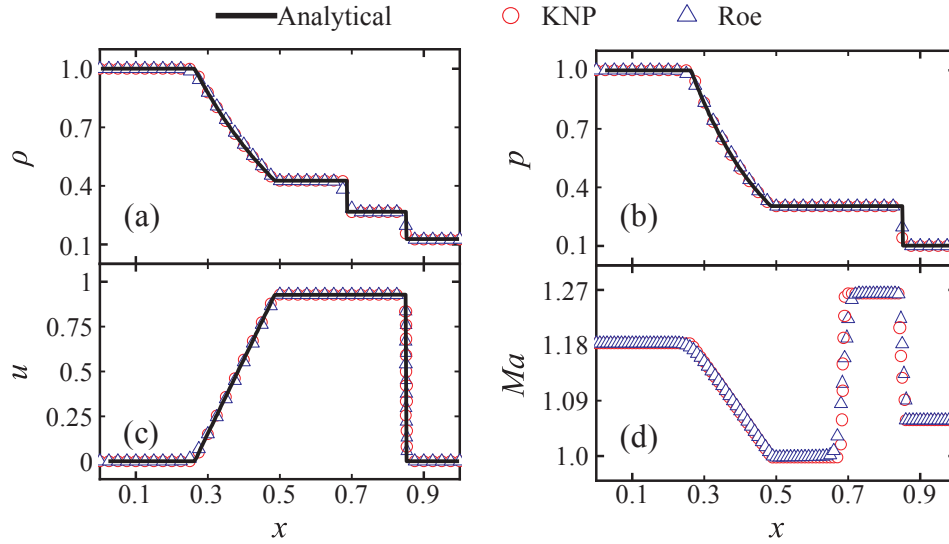


Fig. A1. Comparisons between KNP scheme [5], Roe scheme [7] and analytical solution for the Sod's shock tube problem [54]: (a) density, (b) pressure, (c) velocity and (d) Mach number at $t = 0.007$ s.

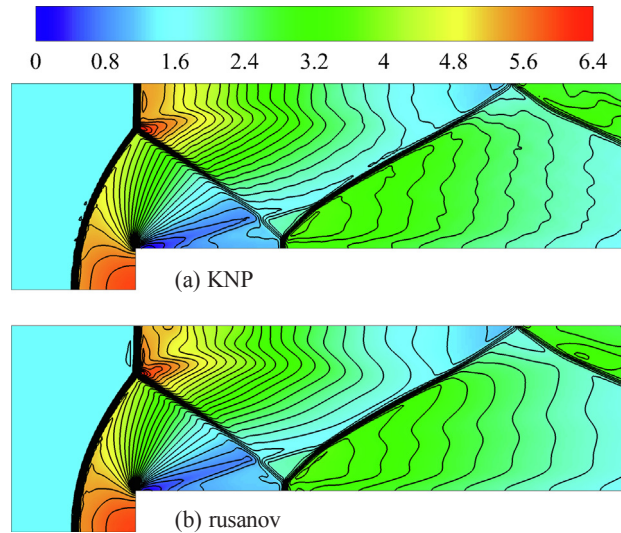


Fig. A2. Comparisons of (a) KNP [5] and (b) Rusanov [55] schemes for Mach 3 flow past a forward step. Curves: 32 iso-lines of density from 0 to 6.4.

left side of the domain. Supersonic inlet conditions (i.e. fixed values for all variables) are applied at the inlet, whereas zero gradient conditions (Neumann conditions) are used at the outlet. Solid walls are assumed at the upper and lower boundaries of the computational domain. A uniform cell size of $12.5 \text{ mm} \times 12.5 \text{ mm}$ is used. The CFL number is 0.02, which corresponds to a time step of about 0.8 ms. Fig. A2 shows the density contours from KNP [5] and the Rusanov [55] schemes at the same instant. It is seen from Fig. A2 that the KNP scheme can capture the shock waves in supersonic flow passing a forward step and the result is close to that with Rusanov scheme.

A.3. Shock-vortex interaction

This case is studied to analyze the KNP scheme [5] in capturing the interactions between shock wave and vortex. The domain is a 2D rectangular with 2 m in length (x -direction, from 0–2 m) and 1 m in width (y -direction, from 0–1 m), which is discretized with a uniform mesh of 400×200 . A stationary shock of 1.1 Mach is positioned normal to the x -axis at $x = 0.5$ m. On its left, the gas velocity (non-dimensional) is $(u, v) = (\sqrt{1.1\gamma}, 0)$, where u and v are respectively the x and y velocity components, while $\gamma = 1.4$ is the specific heat ratio. The non-dimensional temperature and pressure are $T = 1$ and $p = 1$, respectively. The upper and lower boundaries of the domain are assumed to be reflective walls, whereas the left and right ends are outlets with zero gradient conditions for all variables.

A small vortex centered at $(x_v, y_v) = (0.25 \text{ m}, 0.5 \text{ m})$ is superposed to the flow on the left of the stationary shock. The vortex is described as a perturbation in its velocity (u_v, v_v) , temperature (T_v) and entropy (S_v) to the mean flow, which are respectively described by

$$u_v = \epsilon\beta e^{\alpha(1-\beta^2)} \sin\theta \tag{A2}$$

$$v_v = -\epsilon\beta e^{\alpha(1-\beta^2)} \cos\theta \tag{A3}$$

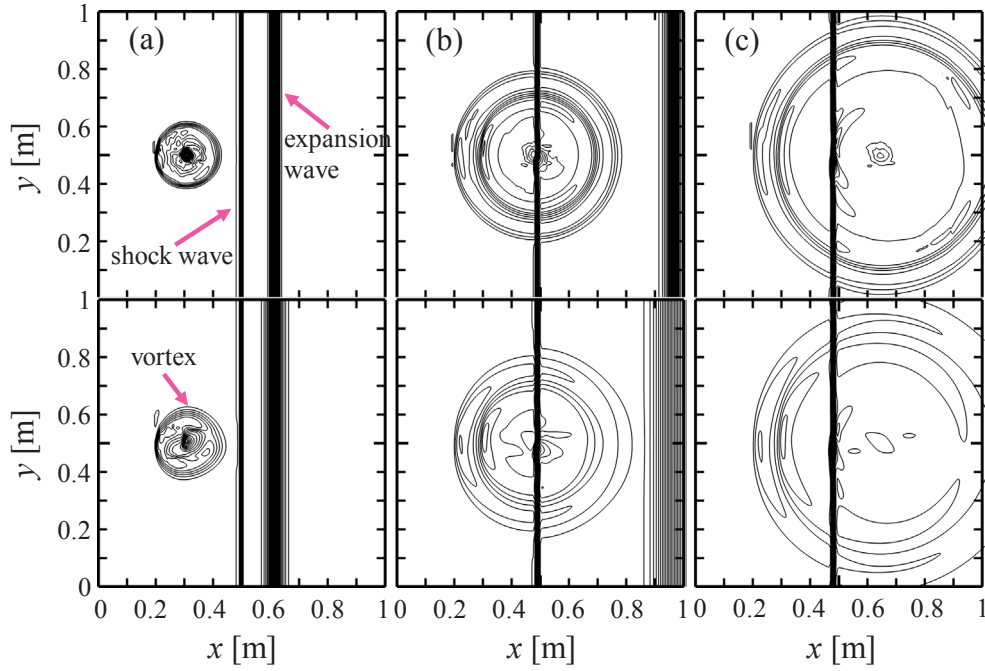


Fig. A3. Evolutions of shock-vortex interactions: (a) $t = 0.05$ s, (b) $t = 0.20$ s and (c) $t = 0.35$ s. The upper row is the result of KNP scheme [5], whilst the lower row from the Roe scheme [7]. Curves: 59 Io-lines of pressure $0.96\text{--}1.25$.

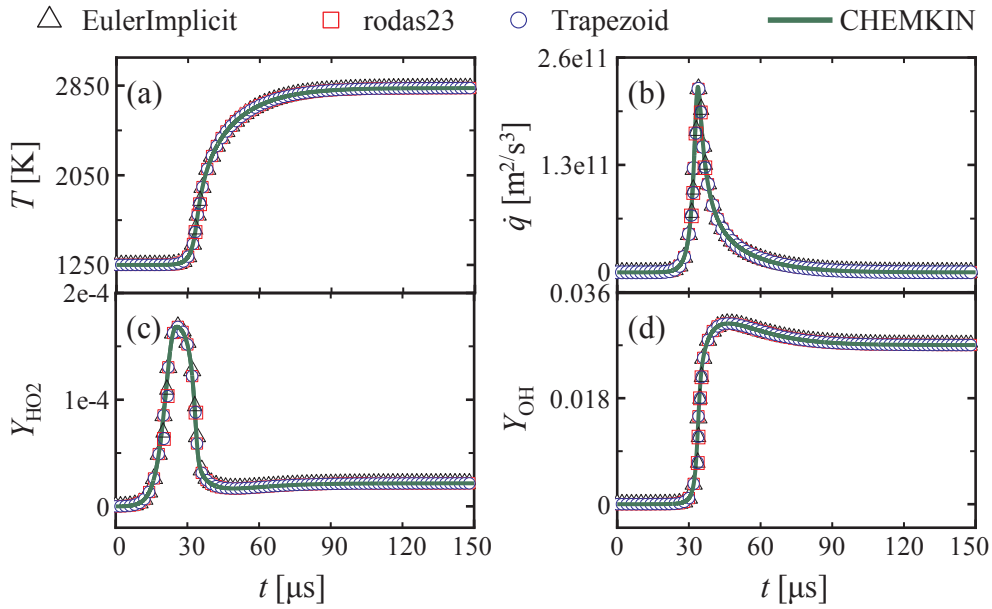


Fig. A4. Comparisons of OpenFOAM ODE solvers and CHEMKIN for auto-ignition of $\text{H}_2/\text{O}_2/\text{H}_2\text{O}/\text{N}_2$ mixture: (a) temperature, (b) heat release rate, (c) HO_2 and (d) OH mass fractions.

$$T_v = -\frac{(\gamma - 1)\varepsilon^2 e^{2\alpha(1-\beta^2)}}{4\alpha\gamma} \quad (\text{A4})$$

$$S_v = 0 \quad (\text{A5})$$

where $\beta = r/r_v$, with $r = \sqrt{(x - x_v)^2 + (y - y_v)^2}$ being the distance to the vortex center and r_v the critical vortex radius for which the vortex strength is maximized. ε indicates the strength of the vortex, α controls the decay rate of the vortex and θ is the angle of point (x, y) to the positive x -axis [56]. In this test, we choose $\varepsilon = 0.3$, $r_v = 0.05$ and $\alpha = 0.204$.

Fig. A3 shows the evolutions of pressure obtained by both the KNP and Roe schemes. It is seen that both the KNP and Roe schemes can well capture the vortex evolution for this problem. However, the KNP scheme shows better performance for the vortex deformation. Furthermore, the KNP scheme gives sharper predictions near the refraction waves, which also shows closer resemblance to the work of Jiang et al. [56].

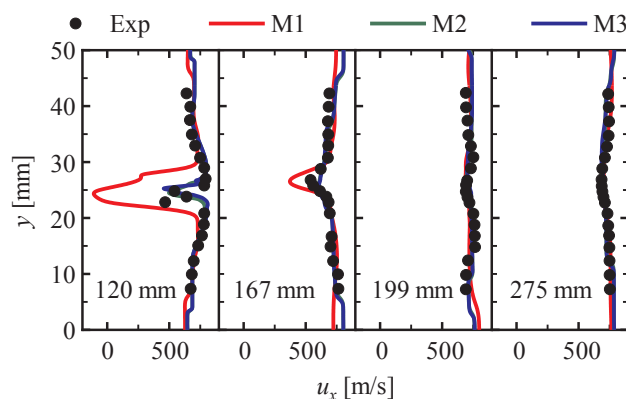


Fig. A5. Profiles of time-averaged axial velocity for the non-reacting flow in the DLR combustor [28].

Appendix B. Comparison of chemistry integration methods

Homogeneous hydrogen autoignition in a constant volume is simulated to examine reaction kinetics calculation and ODE solver accuracy in RYrhoCentralFOAM. The initial temperature and pressure are 1250 K and 110 kPa, respectively. The mixture is composed of $H_2/O_2/H_2O/N_2$, and their molar fractions are 0.2867, 0.1434, 0.1819 and 0.3880, respectively. Such conditions are chosen to mimic those in the supersonic jet flame measured by Cheng et al. [26]. Zero-dimensional calculations are performed (i.e. the physical transport terms are deactivated in energy and species mass fraction equations). A mechanism of 9 species and 19 reactions for hydrogen [57] is used. A single cell with edge of 5 mm is used, and the time step is fixed to be 10^{-9} s. Three chemistry solvers are analyzed, i.e. the first-order Euler implicit solver [58], second-order Trapezoid solver [59] and third-order rods 23 solver [35].

Fig. A4 shows the evolutions of temperature, heat release rate (divided by the constant density in the domain), HO_2 and OH mass fractions obtained from three solvers. Solutions from the Perfectly Stirred Reactor (PSR) solver in the CHEMKIN library [60] are also provided for comparisons, in which the same mechanism and time step are used. It is shown that the accuracies of all the ODE solvers show excellent agreements with that of CHEMKIN.

Appendix C. Mesh sensitivity analysis for DLR supersonic combustor

Fig. A5 shows the distributions of time-averaged axial velocity at different cross-sections for the non-reactive case (flow conditions tabulated in Table 3, but with combustion deactivated) of the DLR supersonic combustor [28]. Three meshes, i.e. M1, M2 and M3, are used for resolution analysis. M2 (4,866,900 cells) has been used for the reactive case in this work, whereas M1 and M3 are two additional meshes respectively with coarser (1,258,500 cells) and finer (7,485,000 cells) cell sizes. It is found from Fig. A5 that differences only can be seen in the recirculation zone for M1, i.e. the central region at $x = 120$ and 167 mm. However, the results from M2 and M3 show good convergence and close to the experimental data. Hence, M2 is used for the reactive case in this study.

References

- [1] Gonzalez-Juez ED, Kerstein AR, Ranjan R, Menon S. Advances and challenges in modeling high-speed turbulent combustion in propulsion systems. *Prog Energy Combust Sci* 2017;60:26–67.
- [2] Weller HG, Tabor G, Jasak H, Fureby C. A tensorial approach to computational continuum mechanics using object-oriented techniques. *Comput Phys* 1998;12:620–31.
- [3] Greenshields CJ, Weller HG, Gasparini L, Reese JM. Implementation of semi-discrete, non-staggered central schemes in a colocated, polyhedral, finite volume framework, for high-speed viscous flows. *Int J Numer Methods Fluids* 2010.
- [4] Kurganov A, Tadmor E. New high-resolution central schemes for nonlinear conservation laws and convection-diffusion equations. *J Comput Phys* 2000;160:241–82.
- [5] Kurganov A, Noelle S, Petrova G. Semidiscrete central-upwind schemes for hyperbolic conservation laws and hamilton-jacobi equations. *SIAM J Sci Comput* 2001;23:707–40.
- [6] van Leer B. Towards the ultimate conservative difference scheme. II. Monotonicity and conservation combined in a second-order scheme. *J Comput Phys* 1974;14:361–70.
- [7] Roe PL. Approximate Riemann solvers, parameter vectors, and difference schemes. *J Comput Phys* 1981;43:357–72.
- [8] Yao W, Lu Y, Li X, Wang J, Fan X. Detached Eddy Simulation of a high-Ma regenerative-cooled scramjet combustor based on skeletal kerosene mechanism. In: 52nd AIAA/SAE/ASEE Jt. Propuls. Conf., American Institute of Aeronautics and Astronautics; 2016.
- [9] Yao W, Lu Y, Wu K, Wang J, Fan X. Modeling Analysis of an Actively Cooled Scramjet Combustor Under Different Kerosene/Air Ratios. *J Propuls Power* 2018;34:975–91.
- [10] Yao W, Wang J, Lu Y, Li X, Fan X. Full-scale Detached Eddy Simulation of kerosene fueled scramjet combustor based on skeletal mechanism. In: 20th AIAA Int. Sp. Planes Hypersonic Syst. Technol. Conf., American Institute of Aeronautics and Astronautics; 2015.
- [11] K. Wu, P. Zhang, W. Yao, X. Fan, LES Study of Flame Stabilization in DLR Hydrogen Supersonic Combustor with Strut Injection, 21st AIAA International Space Planes and Hypersonics Technologies Conference; 2017.
- [12] Wu K, Zhang P, Yao W, Fan X. Numerical investigation on flame stabilization in DLR hydrogen supersonic combustor with strut injection. *Combust Sci Technol* 2017;189:2154–79.
- [13] Cai Z, Wang Z, Sun M, Bai X-S. Effect of combustor geometry and fuel injection scheme on the combustion process in a supersonic flow. *Acta Astronaut* 2016;129:44–51.
- [14] Gong C, Jangi M, Bai XS, Liang JH, Sun MB. Large eddy simulation of hydrogen combustion in supersonic flows using an Eulerian stochastic fields method. *Int J Hydrogen Energy* 2017;42:1264–75.
- [15] Wang Z, Cai Z, Sun M, Wang H, Zhang Y. Large Eddy Simulation of the flame stabilization process in a scramjet combustor with rearwall-expansion cavity. *Int J Hydrogen Energy* 2016;41:19278–88.
- [16] Cai Z, Zhu J, Sun M, Wang Z. Effect of cavity fueling schemes on the laser-induced plasma ignition process in a scramjet combustor. *Aerosp Sci Technol* 2018;78:197–204.
- [17] Cao C, Ye T, Zhao M. Large eddy simulation of hydrogen/air scramjet combustion using tabulated thermo-chemistry approach. *Chinese J Aeronaut* 2015;28:1316–27.
- [18] Zhao M, Zhou T, Ye T, Zhu M, Zhang H. Large eddy simulation of reacting flow in a hydrogen jet into supersonic cross-flow combustor with an inlet compression ramp. *Int J Hydrogen Energy* 2017;42:16782–92.
- [19] Wu W, Piao Y, Liu H. Analysis of flame stabilization mechanism in a hydrogen-fueled reacting wall-jet flame. *Int J Hydrogen Energy* 2019;44:26609–23.
- [20] Galindo-Lopez S, Salehi F, Cleary MJ, Masri AR, Neuber G, Stein OT, et al. A stochastic multiple mapping conditioning computational model in OpenFOAM for turbulent combustion. *Comput Fluids* 2018;172:410–25.
- [21] Zhao M, Zhang H. Large eddy simulation of non-reacting flow and mixing fields in a rotating detonation engine. *Fuel* 2020;280:118534. <https://doi.org/10.1016/j.fuel>.

- 2020.118534.
- [22] Zhao M, Zhang H. Origin and chaotic propagation of multiple rotating detonation waves in hydrogen/air mixtures. *Fuel* 2020;275:117986.
- [23] Huang Z, Zhang H. Numerical investigations of mixed supersonic and subsonic combustion modes in a model combustor. *Int J Hydrogen Energy* 2020;45:1045–60.
- [24] Zhao M, Zhang H. Modelling rotating detonative combustion fueled by partially pre-vaporized n-heptane sprays, Accepted by 38th International Symposium on Combustion, and under review by *Proc. Combust Inst* 2021;38.
- [25] Huang Z, Zhang H. Investigations of autoignition and propagation of supersonic ethylene flames stabilized by a cavity. *Appl Energy* 2020;265:114795.
- [26] Cheng TS, Wehrmeyer JA, Pitz RW, Jarrett O, Northam GB. Raman measurement of mixing and finite-rate chemistry in a supersonic hydrogen-air diffusion flame. *Combust Flame* 1994;99:157–73.
- [27] Alff F, Böhm M, Clauß W, Oschwald M, Waidmann W. Supersonic Combustion of Hydrogen/Air in a Scramjet Combustion Chamber, in: 45th Int. Astronaut. Congr.; 1994.
- [28] Waidmann W, Alff F, Böhm M, Brummund U, Clauß W, Oschwald M. Supersonic combustion of hydrogen/air in a scramjet combustion chamber. *Sp Technol* 1995.
- [29] Poling BE, Prausnitz JM, O'Connell JP. The properties of gases and liquids. McGraw-hill New York; 2001.
- [30] McBride B, Gordon S, Reno M. Coefficients for calculating thermodynamic and transport properties of individual species. National Aeronautics and Space Administration; 1993.
- [31] Fureby C. On subgrid scale modeling in large eddy simulations of compressible fluid flow. *Phys Fluids* 1996;8:1301–11.
- [32] Zhao M, Chen ZX, Zhang H, Swaminathan N. Large eddy simulation of a supersonic lifted hydrogen-air flame with perfectly stirred reactor model, Submitted to *Combust. Flame*; 2020.
- [33] Huang Z, Cleary MJ, Zhang H. Large eddy simulation of a model supersonic combustor with a sparse-Lagrangian multiple mapping conditioning approach, Submitted to *Combust. Flame*; 2020.
- [34] Bader G, Deuflhard P. A semi-implicit mid-point rule for stiff systems of ordinary differential equations. *Numer Math* 1983;41:373–98.
- [35] Sandu A, Verwer JG, Blom JG, Spee EJ, Carmichael GR, Potra FA. Benchmarking stiff ODE solvers for atmospheric chemistry problems II: Rosenbrock solvers. *Atmos Environ* 1997;31:3459–72.
- [36] Dancy C. The turbulent flow field downstream of an axisymmetric Mach 2 supersonic burner-LDA measurements, in: 32nd Jt. Propuls. Conf. Exhib., 1996: p. 3073.
- [37] Schonfeld T, Rudgyard M. Steady and unsteady flow simulations using the hybrid flow solver AVBP. *AIAA J* 1999;37:1378–85.
- [38] <https://www.coria-cfd.fr/index.php/SiTCom-B>, (n.d.).
- [39] Scherrer D, Chedevergne F, G Prenard, Troyes J, Murrone A, Montreuil E, Vuillot F, Lupoglazoff N, Huet M, Sainte B. Rose, Recent CEDRE applications, (2011).
- [40] Moule Y, Sabelnikov V, Mura A. Highly resolved numerical simulation of combustion in supersonic hydrogen-air coflowing jets. *Combust Flame* 2014;161:2647–68.
- [41] Boivin P, Dauplain A, Jiménez C, Cuenot B. Simulation of a supersonic hydrogen-air autoignition-stabilized flame using reduced chemistry. *Combust Flame* 2012;159:1779–90.
- [42] Bouheraoua L, Domingo P, Ribert G. Large-eddy simulation of a supersonic lifted jet flame: analysis of the turbulent flame base. *Combust Flame* 2017;179:199–218.
- [43] de Almeida YP, Navarro-Martinez S. Large Eddy Simulation of a supersonic lifted flame using the Eulerian stochastic fields method. *Proc Combust Inst* 2019;37:3693–701.
- [44] Choi J-Y, Jeung I-S, Yoon Y. Computational fluid dynamics algorithms for unsteady shock-induced combustion, Part 2: Comparison. *AIAA J* 2000;38:1188–95.
- [45] Wu K, Zhang P, Yao W, Fan X. Computational realization of multiple flame stabilization modes in DLR strut-injection hydrogen supersonic combustor. *Proc Combust Inst* 2019.
- [46] Huang Z, Zhao M, Zhang H. Modelling n-heptane dilute spray flames in a model supersonic combustor fueled by hydrogen. *Fuel* 2020;264:116809.
- [47] Wang H, Shan F, Piao Y, Hou L, Niu J. IDDES simulation of hydrogen-fueled supersonic combustion using flamelet modeling. *Int J Hydrogen Energy* 2015.
- [48] Marinov NM, Westbrook CK, Pitz WJ. Detailed and global chemical kinetics model for hydrogen. *Transp Phenom Combust* 1996;1:118.
- [49] Berglund M, Fureby C. LES of supersonic combustion in a scramjet engine model. *Proc Combust Inst* 2007;31(2):2497–504.
- [50] Génin F, Menon S. Simulation of turbulent mixing behind a strut injector in supersonic flow. *AIAA J* 2010;48:526–39.
- [51] Fureby C, Fedina E, Tegnér J. A computational study of supersonic combustion behind a wedge-shaped flameholder. *Shock Waves* 2014;24:41–50.
- [52] Huang Z, He G, Wang S, Qin F, Wei X, Shi L. Simulations of combustion oscillation and flame dynamics in a strut-based supersonic combustor. *Int J Hydrogen Energy* 2017;42:8278–87.
- [53] Fureby C, Alin N, Wikström N, Menon S, Svanstedt N, Persson L. Large-Eddy simulation of high-reynolds-number wall-bounded flows. *AIAA J* 2004;42:457–68.
- [54] Sod GA. A survey of several finite difference methods for systems of nonlinear hyperbolic conservation laws. *J Comput Phys* 1978;27:1–31.
- [55] Rusanov VV. Calculation of interaction of non-steady shock waves with obstacles. *J Comp Math Phys* 1961;279.
- [56] Jiang GS, Shu CW. Efficient implementation of weighted ENO schemes. *J Comput Phys* 1996;126:202–28.
- [57] Curran HJ, Simmie JM, Pitz WJ, Marcus O, Westbrook CK. A comprehensive modeling study of hydrogen oxidation, 36 (2004) 603–622.
- [58] Hairer E, Nørsett SP, Wanner G. Solving Ordinary differential equations I: Nonstiff problems. Berlin Heidelberg: Springer; 1987.
- [59] Hairer E, Wanner G. Solving ordinary differential equations II: stiff and differential-algebraic problems. second ed. Berlin Heidelberg: Springer; 1996.
- [60] Kee R, Rupley F, Meeks E. CHEMKIN-III: a fortran chemical kinetics package for the analysis of gas-phase chemical and plasma kinetics. Sandia Natl. Lab; 1996.